Acta Materialia 166 (2019) 346–356

Contents lists available at ScienceDirect

Acta Materialia

journal homepage: www.elsevier.com/locate/actamat

Full length article

Ultrahigh superelastic damping at the nano-scale: A robust phenomenon to improve smart MEMS devices

Jose F. Gómez-Cortés [a], María L. Nó [b], Isabel Ruíz-Larrea [b], Tomasz Breczewski [b], Angel López-Echarri [a], Christopher A. Schuh [c], Jose M. San Juan [a, *]

[a] Dpt. Física Materia Condensada, Facultad de Ciencia y Tecnología, Universidad del País Vasco, UPV/EHU, Apdo 644, 48080, Bilbao, Spain
[b] Dpt. Física Aplicada II, Facultad de Ciencia y Tecnología, Universidad del País Vasco, UPV/EHU, Apdo 644, 48080, Bilbao, Spain
[c] Dpt. of Materials Science and Engineering, Massachusetts Institute of Technology, 77 Massachusetts Avenue, Cambridge, 02139, MA, USA

ARTICLE INFO

Article history:
Received 11 October 2018
Received in revised form
21 December 2018
Accepted 22 December 2018
Available online 29 December 2018

Keywords:
Shape memory alloys
Cu-Al-Ni
Martensitic transformation
Nanoindentation
Damping capacity

ABSTRACT

Micro and nano pillars of Copper-based shape memory alloys (SMAs) with feature sizes between about 2 μm and 250 nm are known to exhibit ultra-high mechanical damping due to the nucleation and motion of stress-induced martensite interfaces during superelastic straining. While this behavior could be extremely useful to protect micro electro-mechanical systems (MEMS) against vibrations in aggressive environments, a fundamental question must yet be answered in order to envisage further applications, namely, whether this damping is reproducible and stable over long times and many cycles, or whether the damping is a signal of accumulating damage that could compromise long-term usage. In the present paper this crucial question is answered; we show that micropillar arrays of Cu-Al-Ni SMAs exhibit a completely recoverable and reproducible superelastic response, with an ultra-high damping loss factor $\eta > 0.1$, or even higher for sub-micrometer pillars, $\eta > 0.2$, even after thousands of cycles (>5000) and after long times spanning more than four years. Furthermore, the first high-frequency tests on such nanoscale SMAs show that their superelastic response is very fast and relevant to ultra-high damping even at frequencies as high as 1000 Hz. This paves the way for the design of micro/nano dampers, based on SMAs, to improve the reliability of MEMS in noisy environments.

1. Introduction

Among the different functional smart materials, shape memory alloys (SMAs) are able to perform sensing and actuating functions thanks to a reversible thermoelastic martensitic transformation (MT). The mechanism of this first order diffusionless transformation proceeds by a shearing of the atomic lattice of the high-temperature phase (austenite), to produce the low-temperature phase (martensite) [1]. The MT can be thermally induced by cooling, giving rise to the shape memory effect upon reheating, or induced by the application of stress promoting the requisite crystallographic shearing, which is also reversible in what is known as the superelastic effect [2,3]. These thermo-mechanical properties, i.e., the shape memory and superelastic effects, make SMAs one of the most important families of shape memory materials [4], having found a great number of technological applications [5]. In comparison with other functional materials, SMAs exhibit an extremely high work-output per unit volume, up to ~10^7 Jm^{-3} [6], offering a competitive advantage for applications in next generation Smart Micro Electro-Mechanical Systems (SMEMS) [7].

Up to this point, most efforts at integrating SMAs into MEMS have been oriented on SMA thin films, from which many devices, such as microgrippers and microvalves, among others, have been developed for MEMS applications (see the reviews in Refs. [8,9]). A related line of work focuses on the search for new thin film SMA compositions by combinatorial techniques [10–12], which may exhibit required properties such as improved long term functional fatigue [13,14]. And while thin film SMAs present one dimension that is reduced to the nanoscale, newer challenges, driven for example by flexible electronics and wearable health-care technologies, pertain to SMA miniaturization in all 3D dimensions. As a result, there is increasing effort devoted to producing and characterizing micro and nano-scale SMA structures and features. For example, instrumented nanoindentation techniques [15] initially used for the study of confined plasticity [16,17], have been applied

* Corresponding author.
E-mail address: jose.sanjuan@ehu.es (J.M. San Juan).

https://doi.org/10.1016/j.actamat.2018.12.043

to study SMAs at small scale [7,18]. In addition, several sample size-effects on damping behavior [19], on magnetic actuation [20] and on the critical stress for superelasticity [21] were recently discovered; these new phenomena speak not just to miniaturization of the shape memory and superelastic effects, but to previously unforeseen capabilities unlocked only at the scale of SMEMS. Of particular relevance to the present work is the ultra-high damping behavior reported in small-scale SMA pillars [19], which has been proposed as potentially useful to damp mechanical vibrations in MEMS working in extremely aggressive noisy environments. As reliability in the presence of mechanical noise is one of the most important issues [22,23] for the application of MEMS in aerospace, automotive, robotic and bio-medical industries, the use of SMAs seems appropriate; SMAs are intrinsically high-damping materials even at bulk scales [24] especially during superelastic straining [25], with a large enhancement at the small scales relevant to MEMS [19].

There is, however, one significant gap between the proposed use of SMAs as MEMS dampers and the practicality of it, and that pertains to stability of this nanoscale effect over long term cycling and after large lengths of time. In the most widely known family of SMAs, based on Ti-Ni, it has been shown that superelasticity is compromised in small-scale specimens, which often do not fully recover superelastic strains due to premature plasticity [26–29]. Although Cu-based SMA micro and nano pillars [7,19,21,30,31] as well as microwires [32–35] exhibit complete superelastic recovery even after moderate cycling [36–38], there is reason to question the stability of the effect. In particular, the higher level of damping associated with micro- and nanoscale Cu-based SMAs suggests a possibility of accumulating defect energy in the crystalline lattice on every cycle; such structural evolution could very well lead to property evolution or fatigue failure after many cycles.

Thus, explicit study of the long-term stability of the enhanced damping effect in micro- and nanoscale Cu-based SMAs is required as a next step to support application relevance of the concept. A primary purpose of the present paper is to provide such a study and establish the long-term stability of enhanced damping through thousands of cycles and recovered after intermittent testing spanning more than four years. Additionally, throughout the paper we introduce new results on Cu-Al-Ni SMAs that highlight their feasibility as micro-dampers to improve the reliability of MEMS. In particular, we demonstrate reproducibility of SMA behavior across arrays of many micro pillars, and assess the damping response of these structures over a range of frequencies.

2. Materials and methods

Samples were polished plates, 1-mm thick, cut from [001] oriented single crystals of Cu-14Al-4Ni wt%, which were treated at 1173 K for 1800 s and quenched in ice water. The transformation temperatures of the MT were determined by differential scanning calorimetry (DSC) as $Ms = 272$ K, $Mf = 242$ K, $As = 273$ K and $Af = 285$ K (Ms, Mf are martensite start and finish temperatures and As, Af are austenite start and finish temperatures), and were chosen through the control of composition [39] in order to study the superelastic effect at room temperature. Arrays of square micro pillars, as shown in Fig. 1a, were milled by using a focused ion beam (FIB), FEI Helios 650, and a program for 3D nanoprototyping [40]. Cylindrical nano pillars studied in the last section were milled with the same equipment at the SGIKER of the University of the Basque Country. The conditions for milling were 30 kV for the I-beam and decreasing currents for the different milling steps, 80, 40 and 24 pA, followed by finishing steps with 15 and 7.7 pA for cylindrical pillars when they become smaller. This procedure was developed to avoid any noticeable influence of potential Ga damage or contamination [19,21]. The images of the pillars before and after testing were taken with the FIB equipment and also using a scanning electron microscope JEOL 7000F. An atomic force microscope (AFM) Park Systems XE-100 was used in non-contact mode to obtain the topographic images and profiles of the spherical indents at the top of the pillars.

Nano compression tests were performed in an instrumented nano indenter Hysitron TI-950, using a sphero-conical 2-μm radius diamond indenter, according to the procedure developed in previous works [7,30] briefly described in Fig. 1. For the array of micropillars, mechanical tests were conducted in load control, to avoid any potential feedback artifacts, at a loading rate of $500\ \mu N\ s^{-1}$, which means that the complete load-unload nano compression cycle takes place in 5 s (0.2 Hz). In the small pillar studied in the final section, several loading rates were considered, from $80\ \mu N\ s^{-1}$, for a full loading in 1 s (0.5 Hz), up to $2250\ \mu N\ s^{-1}$ for a full loading in 0.035 s (14 Hz), and the acquisition rate was increased accordingly, in order to have a reasonable density of points during the martensitic transformation; the time elapsed in between two consecutive points was about 10^{-4} s.

For multiple-cycle compression tests, groups of 5 cycles were conducted at a time, accumulated over the first 200 cycles. After this, groups of 20 cycles were used to further accumulate hundreds or thousands of cycles. The purpose of grouping cycles in this manner is described in Refs. [36,38]; it helps maintain a stable, fixed contact point between tip and specimen, and allows local correction of drift displacements. Especially for long-term cycling studies, thermal drift must be carefully controlled and monitored. The equipment, housed inside a thermal/acoustical enclosure, was used in an air-conditioning room with the temperature measured continuously in the chamber near the transducer; 300 ± 1 K was maintained for all the nano compression tests carried out here, over five years. Drift was analyzed before each group of compression cycles, and used to correct the displacements measured over those cycles. For longer tests, periodic re-centering of the indenter tip was occasionally required to avoid the development of a toe-in effect due to the lateral displacement of the settling point [36]. In-situ nano-compression experiments for the observation of the stress-induced martensite variants were performed using a Hysitron Picoindenter PI-85 inside the chamber of the JEOL 7000F. The stage was tilted 25° to allow real-time image acquisition during the tests, and in this case a flat diamond indenter was used.

3. Superelastic damping

The present investigation focused on a Cu-14Al-4Ni wt% SMA, at which concentration the martensitic transformation occurs below room temperature; when testing at room temperature, the material thus exhibits superelastic behavior. To avoid any influence of the microstructure, oriented [001] single crystals were used, and, to enable a systematic study, several arrays of square pillars were milled by FIB, as shown in Fig. 1a. The damping behavior at the nano scale was determined by nano-compression tests using an instrumented nanoindenter, which is also able to work as a scanning probe microscope (SPM) in contact mode. For mechanical testing, first, the square array (18 μm on each side) is imaged in SPM mode, Fig. 1b, and the top of each square pillar (1.7 μm wide and 3.3 μm tall), Fig. 1c, is identified by SPM and centered beneath the indenter, Fig. 1d. Then, a series of nano-compression tests at increasing maximum load is conducted in order to reach the required load for the stress-induced MT, and to establish the so-called “settling point”, Fig. 1e. The settling point is associated with the indenter tip producing local plastic deformation at the contact site, as shown in Fig. 1f. The depth of the plastic contact site is measured in Fig. 1g, and corresponds to the accumulated unrecovered strain measured during the series of nano compression tests in Fig. 1e. The indents

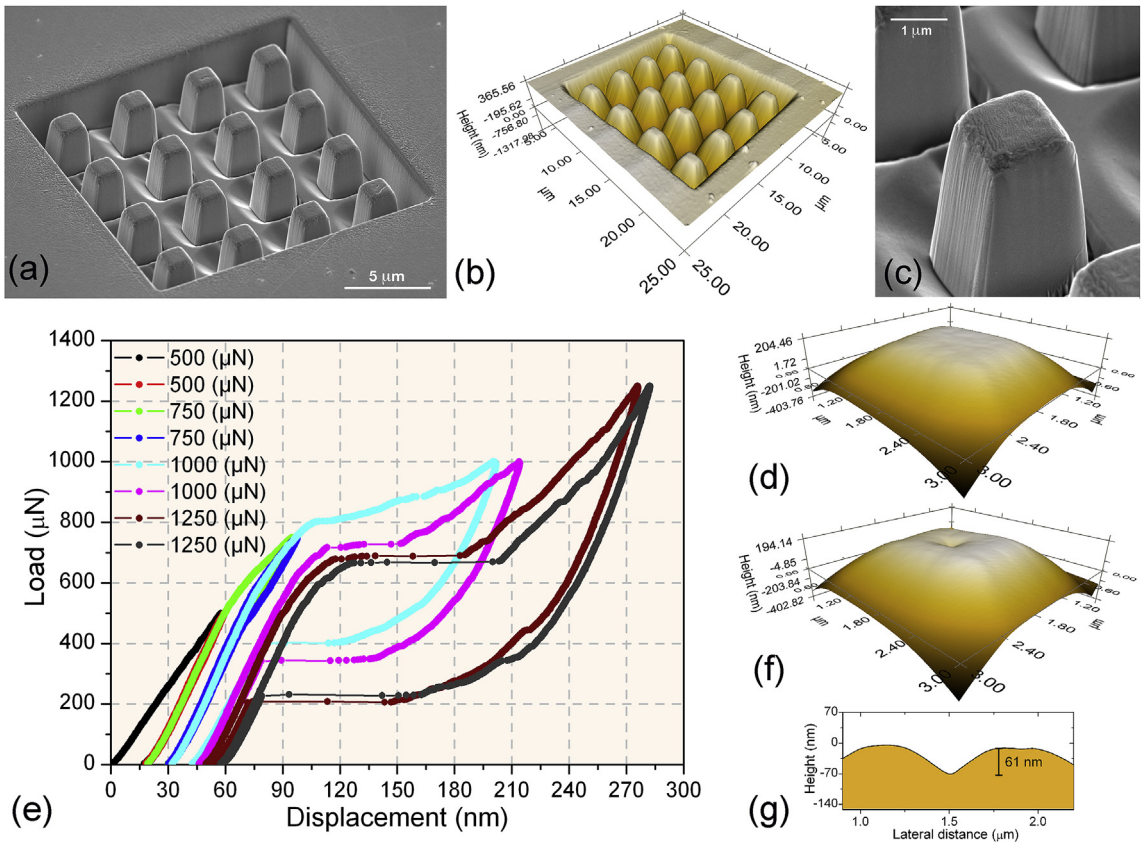

Fig. 1. (a) Scanning electron micrograph of the array of SMA pillars milled by focused ion beam. (b) Image of the array taken in scanning probe imaging mode using the nano-indenter. (c) Detail of one of the pillars. (d) Image of the top of the pillar taken before the nano-compression test. (e) First series of nano-compression tests at increasing maximum load, to identify the critical stresses associated with superelastic behavior, and to establish the settling point. (f) Image of the indentation at the pillar surface after the compression tests. (g) Profile of the indenter showing the residual penetration depth, which corresponds to the unrecovered strain in (e).

produced by the sphero-conical diamond indenter at the top of the pillars were measured by AFM and an example is presented in the Supplementary Figs. S1a and S1b. However, during nano compression tests, the image of the indent is acquired using the same sphero-conical indenter and a geometrical artifact is produced, as explained in Supplementary Fig. S1c; the measured indent of Fig. 1g shows a correct maximum depth but its profile looks sharper than the real spherical indent. Once the sphero-conical indenter has settled into the top of the pillar, its shape is accommodated and during subsequent loading the micropillar experiences essentially uniform compressive load, undergoing completely reversible behavior over many cycles. It should be noted that the taper of the pillars would be responsible for a slight variation of the compressive stress along the height of the pillar. Thereafter, a fully closed load-unload cycle and a completely recoverable superelastic effect is obtained (black dots in Fig. 1e). The superelastic straining of the pillar is due to the stress-induced MT from the cubic β_3 ($L2_1$ ordered) austenite [41], to the orthorhombic γ'_3 (Pmmn) martensite [42], as expected in a compression test in these alloys [43].

3.1. Reproducibility of damping in micro-pillars

The above procedure was applied to all pillars of the array, which exhibit a similar superelastic behavior during the first cycle after settling, as shown in Fig. 2. While the qualitative shapes and trends are all common, there is also evidence of some individuality, presumably due to milling and settling particularities. After reaching the critical stress to induce the MT, a primary set of similarly oriented martensite variants nucleates and propagates very fast across the pillar, giving rise to a plateau of about 3% superelastic strain, followed by a secondary stage exhibiting hardening through the further progress of the MT. The initial nucleation of the martensite, as well as the transition from the primary to the secondary stage, are stochastic effects that could be expected to depend on the local microstructure and surface aspects; this is another reason why each pillar exhibits some individuality and will be further analyzed in the next section.

In a first testing campaign, all pillars were cycled more than 200 times, and with a few exceptions to be described later (P2, P6, P11 & P12) they exhibit similar superelastic behavior. In Fig. 3a the superelastic cycle numbers 1, 100 and 200 are presented for three pillars, P3, P8 and P15, as an example. The critical stress for the stress-induced MT slightly decreases over the first hundred cycles as expected for micron-sized pillars undergoing a training or shakedown process [36]. For pillars above 1 μm diameter, as in the present case, the stress-induced MT is driven by heterogeneous nucleation of martensite on lattice defects (preferentially dislocations) pre-existing or created beneath the indenter during cycling; this has been proposed as leading to the evolution of the critical stress towards the one measured in bulk crystals [21,36] in pillars such as these. However, after 200 cycles of training, a remarkable similarity between the superelastic cycles is observed in Fig. 3b for the three pillars. This is the general behavior observed in most of pillars of the array, which are shown after those 200 nano compression tests in the supplementary material (Fig. S2).

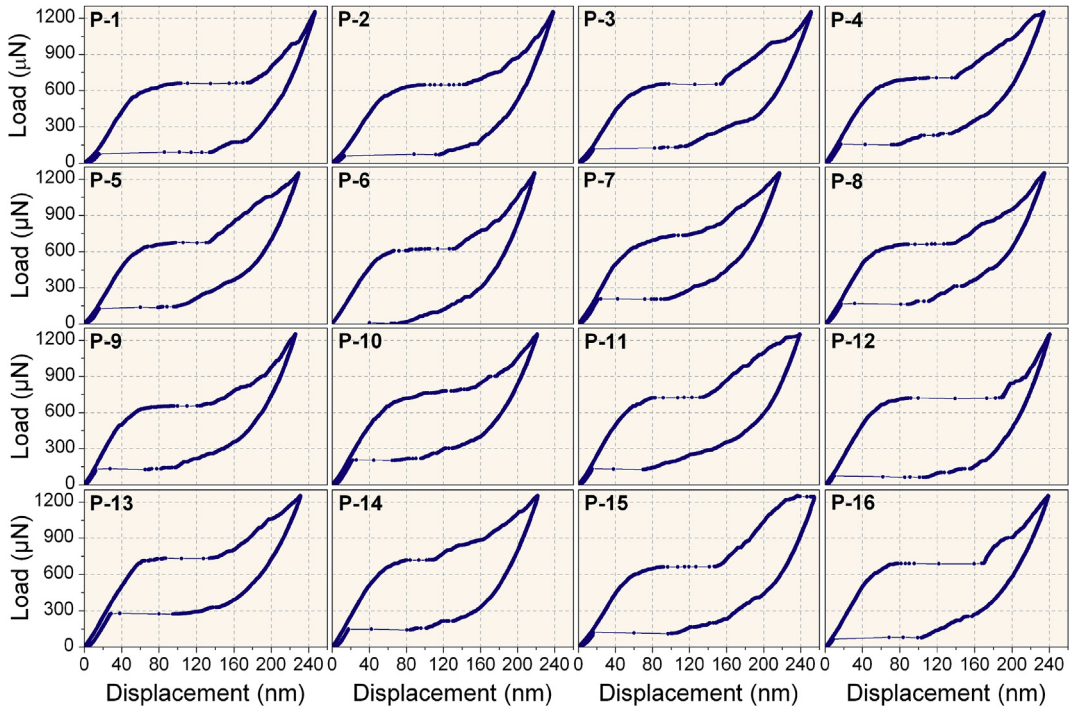

Fig. 2. Load-displacement curves for the first superelastic cycle on each pillar, P-1 to P-16, of the array shown in Fig. 1a.

As noted earlier, four of the pillars, P2, P6, P11 and P12, exhibited a unique behavior. While they initially showed a similar superelastic behavior spanning many cycles, they eventually became stabilized in martensite and did not revert during unloading after 160, 178, 94 and 70 cycles respectively. This is not an entirely unexpected behavior, because the size-effect for ultrahigh mechanical damping has been partially attributed to the release of elastic energy stored at the growing interface between martensite and austenite [19]. In small pillars [7], as well as in microwires [44], martensite plates span completely across the cross-section of the sample, releasing stored elastic energy at the surface. In bulk SMAs, stored elastic energy provides substantial driving force for the reverse MT, and the stress relief in small samples due to the proximity of free surfaces therefore can stabilize martensite, which has less elastic driving force to move back on unloading. When the load during the reverse MT is intrinsically low, training can shake down the reverse transformation stress to a point where it is below zero, i.e., the induced martensite can eventually become stable and martensite plates remain pinned at the surface of the pillar. In the case of our particular Cu-Al-Ni alloy this effect is also prone to happen because of the proximity between the A_f temperature (285 K) and the testing temperature (300 K). This martensite stabilization can be easily avoided, for technological applications, by choosing a slightly different alloy composition such that it would transform at slightly lower temperatures [39].

For nonlinear behaviors such as the superelastic effect, mechanical damping can be measured through the specific damping coefficient defined as [45]: $\Psi = \Delta W/W_{Max}$, with $W_{Max} = \int_0^{\sigma_{Max}} \sigma \cdot d\varepsilon$ being the maximum stored energy per unit volume, and $\Delta W = \oint \sigma \cdot d\varepsilon$ the enclosed area of the hysteresis loop, which represents the dissipated energy per cycle, during the stress-strain (σ-ε) cycle. To compare the results with other dynamic damping measurements under sinusoidal stress, the loss factor $\eta = \Delta W/2\pi \cdot W_{Max} \approx \tan(\phi)$ or the internal friction, $\tan(\phi)$, (with ϕ being the lag angle between the strain and the stress) are used [45,46]. However, when only a positive strain-stress cycle is considered, as in the present case, the cyclic integral extends only over a half cycle and the lost factor is defined as [46]:

$$\eta = \frac{\Delta W}{\pi \cdot W_{Max}} \tag{1}$$

In principle, both integrals ΔW and W_{Max} should be calculated over a stress-strain cycle and over the pillar volume, requiring a precise measurement of the cross-sectional area and height, which is complicated by the taper of pillars. Fortunately, the loss factor η is an intensive magnitude, representing the dissipated energy per unit volume per cycle, which is not, in its definition, dependent on the sample shape. Indeed, as both integrals ΔW and W_{Max} scale in the same way, the loss factor defined by equation (1) can be evaluated through integrals over the load-displacement curves, following the schema of Fig. 4a.

The loss factor measured for cycles 1 and 200 of all pillars is represented in Fig. 4b. The error bars do not correspond to the specific uncertainty for each pillar, which is much smaller, but to the standard deviation about the mean value of η, which is $\eta = 0.18 \pm 0.02$ and $\eta = 0.16 \pm 0.02$ for cycles 1 and 200 respectively. At this point we observe that even after 200 cycles, these pillars exhibit ultrahigh mechanical damping, because High Damping Metals (HIDAMETS) are considered as those exhibiting a loss factor above 0.01 [47].

3.2. Ultra-high mechanical damping during long-term cycling

The reliability of MEMS could be improved by micro dampers to resist inertial effects of high amplitude structural vibrations. However, in many applications such damping is not persistently required, but rather only needed during particularly aggressive noisy events, like the launching of a rocket, an unexpected impact or sudden fall of a person wearing a bio-MEMS device, for instance. Our simulation of such conditions is provided by a long-term

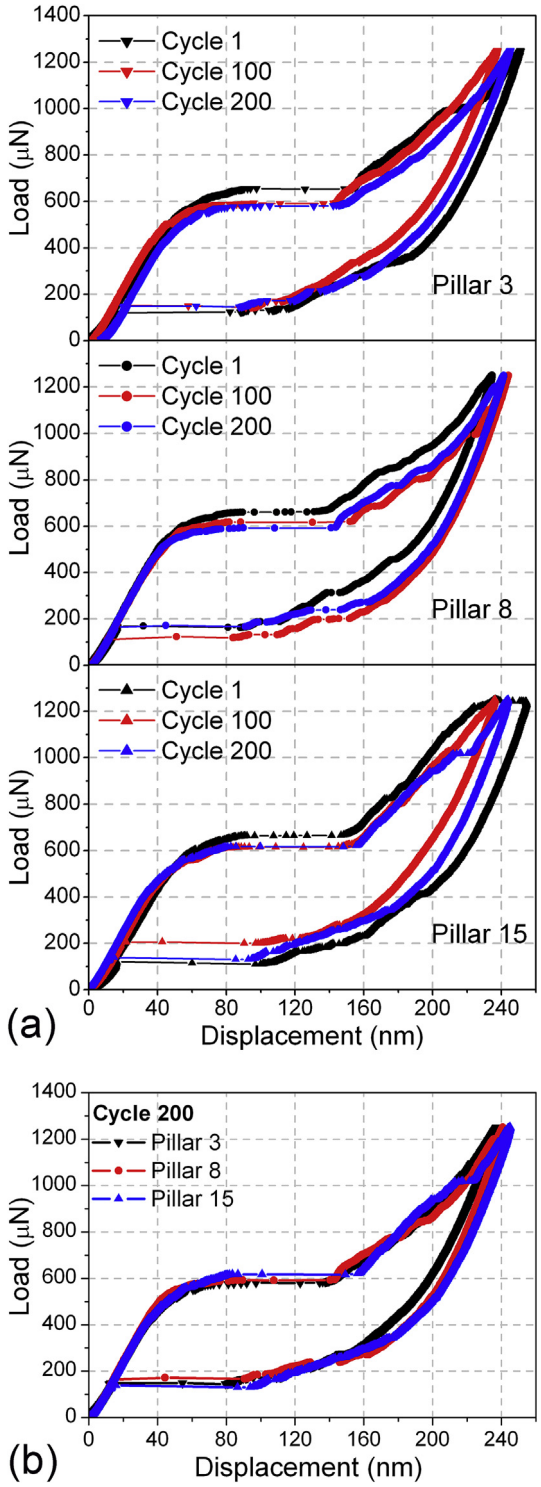

Fig. 3. (a) Superelastic cycles 1, 100 and 200 for three selected pillars, numbered 3, 8 and 15. (b) Comparison of the 200th superelastic cycle for the three indicated pillars, showing the reproducibility of cycling.

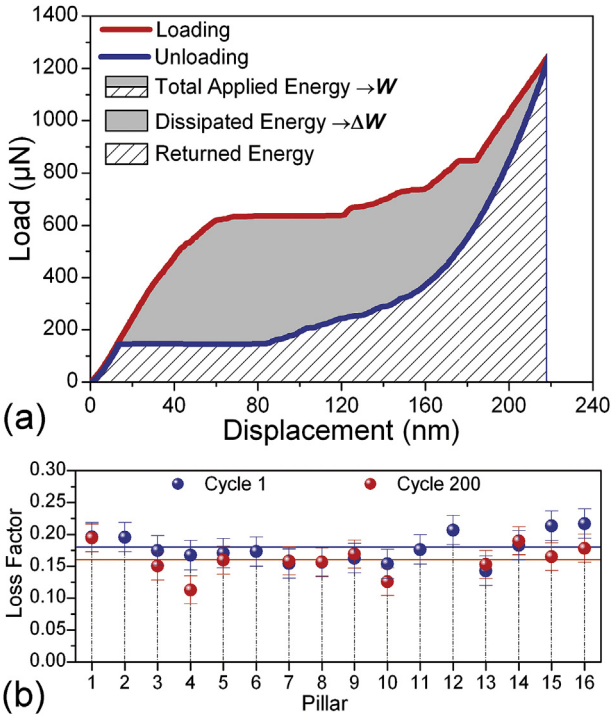

Fig. 4. (a) Schematic showing the different energy terms used to measure the loss factor from a superelastic nano-compression test. (b) Loss factor measured for all pillars of the array shown in Fig. 1, during the first cycle (blue dots) and the 200th cycle (red dots). (For interpretation of the references to color in this figure legend, the reader is referred to the Web version of this article.)

cycling study structured in three intermittent campaigns carried on over more than four years, in which the damping of some selected pillars was measured over several thousand cumulative cycles. Pillars P1, P7 and P10 were selected for these three campaigns and in Fig. 5, the first (black points) and last (blue points) superelastic cycles of each campaign, as well as another intermediate one (red points), are plotted for each of these pillars. Over the course of testing, pillars P1, P7 and P10 accumulated 5020, 2102 and 3230 cycles respectively, and measurements were stopped without any noticeable degradation of the superelastic behavior. The evolution from the first superelastic cycle at the beginning of the first campaign was discussed earlier in terms of the development of the settling point beneath the indenter. The first cycles of the second and third campaigns, after long-term storage of the sample, show an anomalous superelastic curve with a higher load plateau, which evolves very quickly (in a few cycles) to the "normal" superelastic cycle matching that at the end of the prior campaign. This evolution is shown in the supplementary material, Fig. S3. This is attributed to the formation, during storage, of a thin native oxide film over the pillars, which is broken during a new "settling" phase that occurs during the first superelastic cycles. A new accommodation to the settling point is very occasionally required simply because the contact in a given campaign is slightly different from that in the prior one, producing some local deformation responsible for a toe-in effect during the first few cycles [36]. To illustrate the above explanation, the image of the array at the end of the third campaign, to be compared with Fig. 1 taken at the beginning, is included in the supplementary material, Fig. S4. In spite of some degradation of the pillars' surfaces, it is worth noting the exceptional reproducibility of the superelastic behavior in all pillars; compare cycles 1010 and 2020 in pillar P10, or cycles 4000 and 5020 in pillar P1, for instance.

The lost factor η was measured following the method described in Fig. 4a, for the different series of nano compression tests performed over the three campaigns, and in Fig. 6a the evolution of η is plotted for pillars P10 and P1. Not only is an ultrahigh damping coefficient $\eta > 0.1$ retained after thousands cycles, but it also that remains latent and is readily retrieved after years of ambient

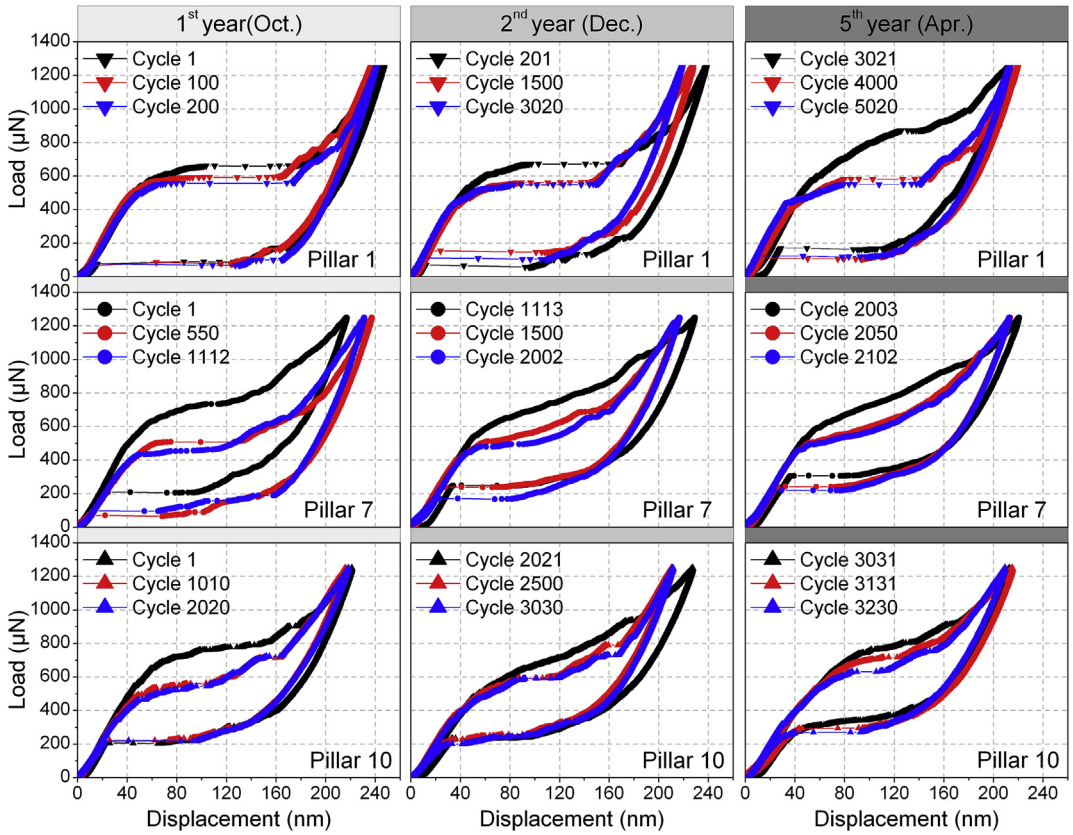

Fig. 5. Superelastic cycling behavior spanning three testing campaigns performed in the first, second and fifth years of the experiment, for three selected pillars P-1, P-7 and P-10. In each graph, the first cycle, the last cycle and one intermediate cycle are indicated.

storage. In Fig. 6b, the different energy terms of the superelastic cycle have been calculated for pillar P1 as a function of the number of cycles. Again, the load-displacement curves were integrated in real units μN (load) and nm (displacement) to obtain the mechanical energy in joules J, and energy densities (J m^{-3}) were obtained using the measured volume of the pillars. Fig. 6b shows that over 5000 cycles, the dissipated energy is almost half of the total applied energy, and the mechanical energy dissipated per unit volume maintains a remarkable value of about 7×10^6 J m^{-3}. Taking into account that the complete loading-unloading cycle takes place in 5 s (0.2 Hz), it can be concluded that each pillar offers a high density of dissipated mechanical power of about 1.5 MW m^{-3}.

In spite of the excellent reversibility of the superelastic cycle, it could be argued that a careful observation of Fig. 5 reveals a slight but progressive evolution of the load-displacement curves on cycling, which is associated with a very small, but still measurable, decrease of the loss factor for the long-term cycling shown in Fig. 6a. The main parameters characterizing this gradual evolution during cycling include (a) a slight decrease in the maximum superelastic strain achieved, as well as (b) a relative decrease of the extent of the transformation plateau stage with respect to the hardening stage. Taking as reference pillar 1 in Fig. 5, the superelastic plateau extends over more than 170 nm displacement for cycle 200, and progressively reduces to about 140 nm for cycle 5020, with a similar evolution occurring in the reverse transformation plateau on unloading. Interestingly, the hardening stage just after the plateau maintains roughly the same shape and extent. This means that the decrease of the plateau length is responsible for the entire net effect of decreasing superelastic strain, and consequently for the slight reduction of the loss factor. To understand the origin of this evolution, a deep analysis of the stress-induced martensite microstructure is required.

New arrays of square cross-section pillars were milled by FIB on the same [001] oriented sample, but in a geometrical configuration allowing observation of the flat lateral side of the pillars in a JEOL 7000F SEM. Such observations were made in situ while performing a nano-compression test using the Hysitron Picoindenter PI-85. Fig. 7a shows a linear array of such pillars on which nano-compression tests were performed, as in Fig. 7b. During the test, video was recorded, but as the quality of these high-scan-rate images was insufficient for detailed analysis, the test was interrupted under load in order to take a high quality image of the stress-induced martensites. The best contrast was obtained in secondary electron mode and Fig. 7c shows the two different sets of stress-induced martensite variants. The primary set corresponds to the best-oriented variants with the highest basal plane Schmidt factor, which is responsible for the variant selection at small scale as shown in transmission electron microscopy (TEM) in-situ experiments [48]. The striped pattern of the primary set of martensite variants that span the entire micro-pillar is clearly seen in Fig. 7c. The shear strain associated with this set of variants, projected onto the pillar axis, corresponds to the superelastic strain plateau, taking place very quickly under practically constant stress. In principle, the shear strain of these transformation variants should produce a lateral displacement of the top of the pillar with respect to the bottom, which we do not observe in Fig. 7. This is presumably because the rigid constraint of the indenter contact at the settling point prevents such displacement. Consequently, such constraint leads to the development of lateral stresses emerging, triggering a secondary set of martensite variants, geometrically compatible

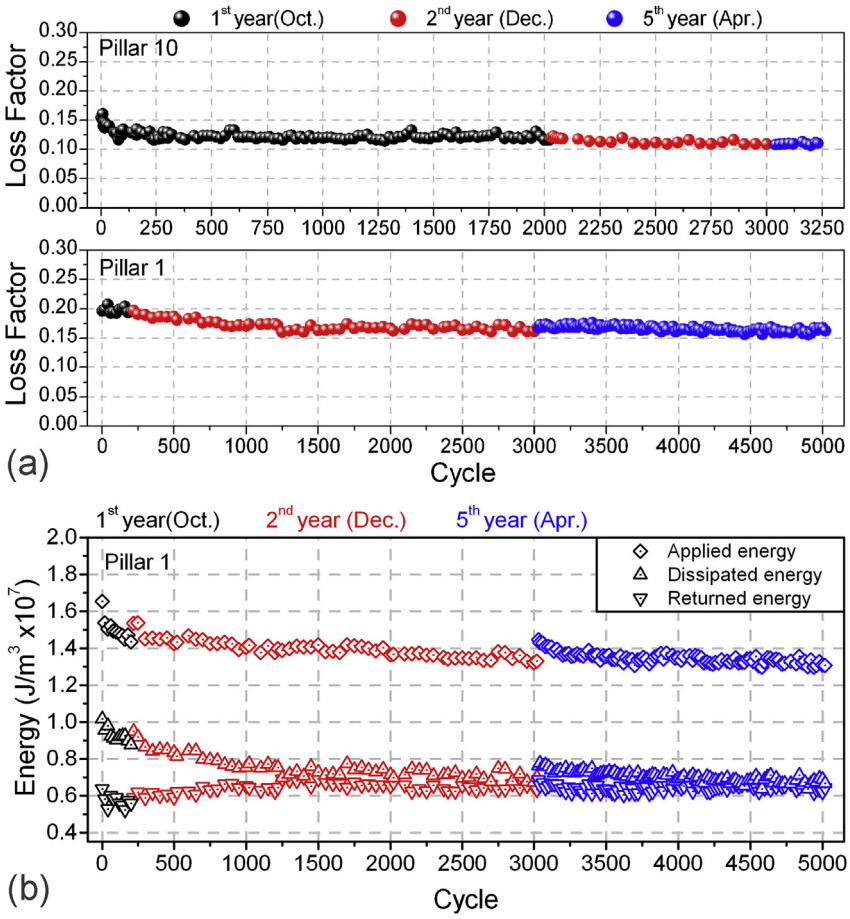

Fig. 6. (a) Evolution of the loss factor for pillars P-10 and P-1 measured over 3230 cycles and 5020 cycles respectively. The dot colors, black, red and blue, correspond to the measurements performed during each of the three campaigns. (b) Evolution of energy density for each of the three energetic terms considered when measuring the loss factor, in the case of the pillar P-1; color code is the same as in (a).

with the local stresses influenced by the platen constraint. This secondary set of variants, which is also clearly seen in the image of Fig. 7c, is associated with the strain hardening stage that appears just after the superelastic plateau.

Upon unloading, the reverse MT takes place and the pristine surface of the pillars is recovered in Fig. 7d. Although each cycle apparently shows completely reversible superelasticity, the intersection of the primary and secondary set of martensite variants upon cycling is expected to generate dislocations, as observed by TEM in similar bulk single crystals [49]. This provides a mechanism for substructure evolution; each cycle of transformation can produce some dislocation activity that grows to interfere with the rapid transformation of the primary set of variants, decreasing the extent of the strain plateau and thus slightly decreasing the loss factor. In this scenario, one possible line of action that could be suggested to avoid such evolution would be to limit the applied strain so as not to exceed the plateau stage (~3%). This is a realistic practical requirement taking into account that long-term fatigue behavior in Ti-Ni alloys recently reported [13,14] was obtained for a superelastic strain below 1.5%. However, we suggest that a still more favorable scenario is possible when working with nanopillars.

3.3. Dependence of loss factor on size

The loss factor during the stress-induced MT is intrinsically non-linear with both the applied stress and the imposed strain. Thus, a comparative study of the loss factor as a function of pillar size requires equivalent experimental conditions during testing. This is a tricky task because a strong size-effect has been reported on the critical stress for superelasticity [21], which increases when decreasing the diameter of the pillars below ~1 μm. In Fig. 8 a,b,c three nanopillars of ~620, 310 and 270 nm diameter are shown, together with their respective stress-strain curves (Fig. 8 d,e,f) measured in each case during the 25th cycle. Indeed, for such small pillars the critical stress for superelasticity increases at smaller diameters and the stress-induced MT occurs very abruptly, which has been associated with homogeneous nucleation [21]. The superelastic plateau develops very quickly (in about 10^{-3} s), preventing experimental control of the superelastic strain, which would be required for systematic measurement of the non-linear loss factor in equivalent conditions across different pillars. In addition, in the case of nanopillars, the plateau associated with the primary set of martensite variants is exhausted at higher and higher strains of 4.3, 5.6 and 6.1% respectively, after subtraction the elastic strain, and the hardening stage associated with secondary martensite variants is absent.

The corresponding values of the loss factor are also indicated for each pillar in Fig. 8, and it can be concluded that nano and sub-micrometer pillars exhibit loss factors that are similar to or perhaps higher than larger pillars, owing to the increase of the critical stress for the stress-induced MT and the decrease of the stress at which the reverse MT occurs. However, the inherent

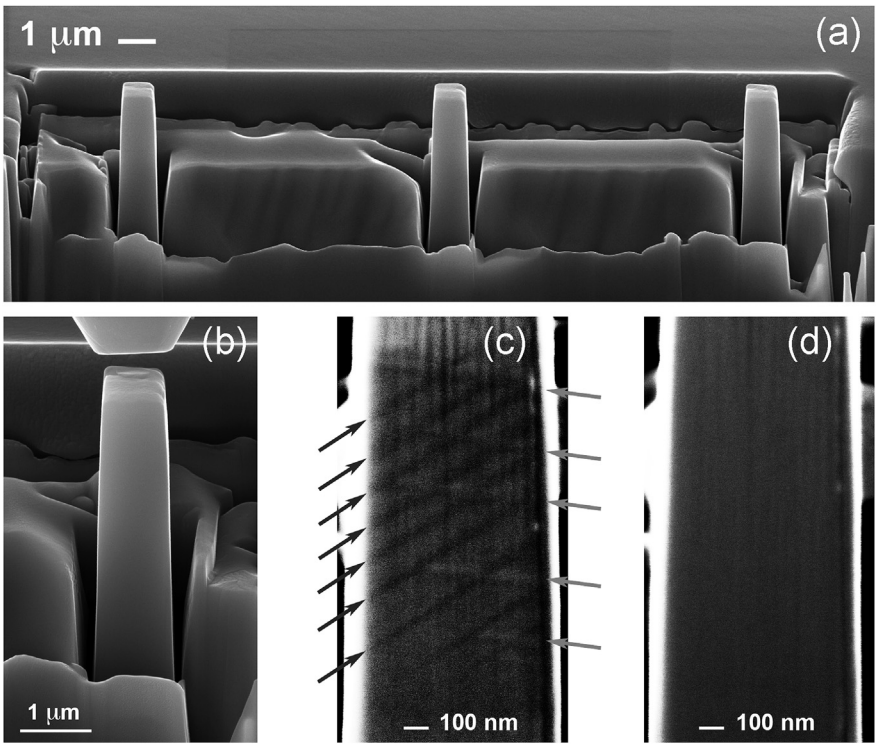

Fig. 7. (a) SEM image of the linear array of pillars milled by FIB to allow lateral observations during compression testing. (b) Detail of the right pillar with the flat indenter just before the in-situ nano-compression test in the Hysitron PI-85. (c) SEM image taken under load during the in-situ test; black arrows on the left indicate the traces of the primary set of martensite variants and grey arrows on the right indicate the traces of the secondary set. (d) Pristine surface of the pillar after withdrawing the applied stress at the end of the in-situ test.

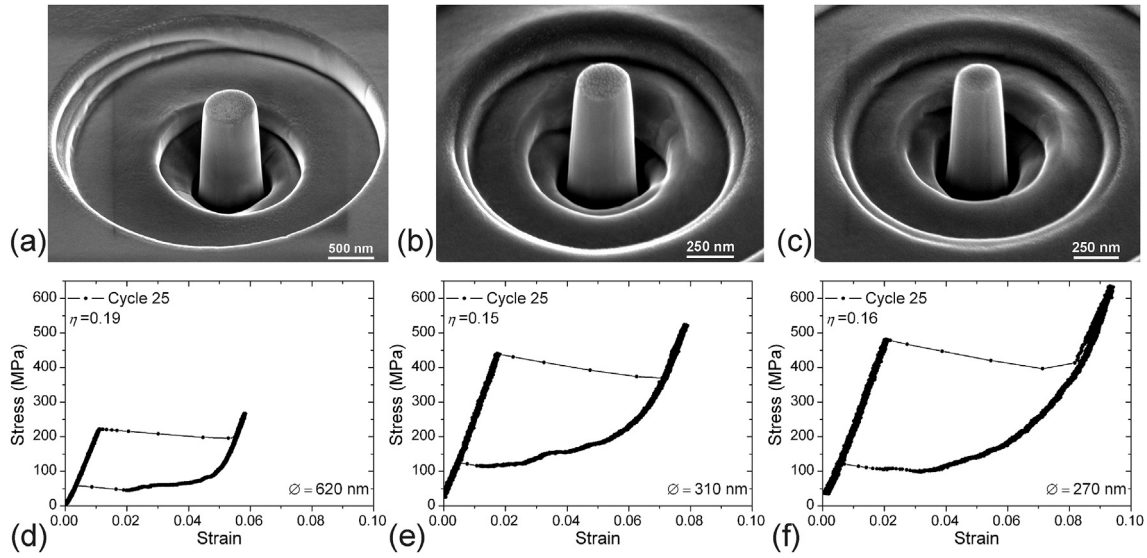

Fig. 8. (a), (b) and (c) are SEM images of nano pillars of 620, 310 and 270 nm in diameter respectively. (d), (e) and (f) are stress-strain curves measured during nano-compression tests (cycle 25) for the corresponding pillars above. Loss factor is also indicated in all cases.

experimental difficulties associated with the non-linear behavior of the loss factor, as well as the individuality of pillars as described above, prevent us from establishing any clear trend with respect to the size of the pillars. The important point is that the long-term reproducibility of the superelastic cycle of nano pillars is expected to be better than the one for micro pillars [21,36], because small pillars undergo the stress-induced MT at much lower loads and generally accumulate less plastic deformation at the contact site. In addition, in nanopillars the development of secondary variants is suppressed or delayed to very high strains, hence no interaction between primary and secondary martensites is expected and consequently dislocations will not be created at the intersections. Thus, superelastic cycling in nanopillars in principle can avoid virtually any plastic deformation, which bodes well for improved cycling behavior.

3.4. Frequency response

Another important aspect to be analyzed is the dependence of the loss factor on frequency. Indeed, if we envisage applying SMA micro devices to protect MEMS against mechanical vibrations, particularly those coming from the natural resonant frequencies of the supporting structures, it could be an engineering requirement that micro dampers exhibit a high loss factor at such frequencies. The intrinsic damping in MEMS is generally attributed to a squeeze-film damping effect related to viscous friction in the air film surrounding mobile parts of the MEMS [50]. However, squeeze-film damping has deleterious effects on the sensitivity and performance of many MEMS devices, like electrostatic actuators, vibrating gyroscopes, optical switches or micro/nano mechanical resonators for instance Ref. [51]. For this reason, it is desirable to eliminate squeeze-film damping, for example by packaging a device in vacuum [52], which can also help alleviate oxidation mechanisms responsible for premature fatigue of silicon structures [53–55]. However, vacuum packaging, by suppressing air squeeze damping, exacerbates the mechanical vibration problem, by improving the transmission of vibrations from the working environment to the moving parts of MEMS. Such vibrations thus are considered to constitute perhaps the most important issue for MEMS reliability [22].

Our results show that SMAs in small volumes may exhibit the long-term ultra-high damping behavior needed to protect MEMS through passive damping of vibrations or shocks. An analysis of the natural frequencies in different specific MEMS structures is out of the scope of the present paper, but it is instructive to consider an example such as spacecraft MEMS applications. Launch vehicle manuals specify minimum values for the fundamental vibration frequency of the payload, in order to avoid dynamic coupling between low-frequency modes of the launcher and the payload spacecraft. For Ariane 5, for instance, the first fundamental lateral and longitudinal frequencies are specified to be $\geq$ 10 Hz and $\geq$31 Hz respectively [56]. Similar frequencies are specified for different launchers [57], and in general a significant response of primary and secondary structures to mechanically transmitted low-frequency vibrations from the launch environment typically occurs below 80 Hz [58].

Thus, application relevance for SMA micro/nano devices in this context requires that we evaluate the loss factor as a function of frequency on the order of perhaps ~10 Hz. Accordingly, superelastic cycles were carried out at increasing frequencies on several nano pillars. As an example, Fig. 9a shows the superelastic cycles carried out in similar conditions as those of Fig. 1 array, on the pillar 620 nm in diameter and 1570 nm in height shown in Fig. 8a, after several hundred previous cycles. Because of the size of the pillar, the critical load for the stress-induced MT is rather low at 65 μN, and the complete cycle takes 2 s (0.5 Hz). The plateau of superelastic strain represents a very rapid event where more than 4% strain develops over 10^{-3} s. The loss factor measured for these cycles is $\eta = 0.21$, a value even higher than the one previously reported at the beginning of the cycling process for the same pillar. Then, in Fig. 9b and c, results are shown for subsequent superelastic test series performed on the same pillar at 8 Hz and 14 Hz respectively. Here the first and last cycles of a series of 5 cycles are shown, for comparison with the standard 0.5 Hz results in Fig. 9a. The reproducibility of the superelastic cycle is very good and the loss factor very high, but in addition the stress-induced MT takes place so fast that the inertial mass of the electrostatic transducer, 150 mg, is not able to follow the motion. Indeed, the observed oscillations mean that the transducer rebounds on the top of the pillar when reaching the maximum strain during the forward MT, and loses contact with the pillar due to inertia at the end of the reverse

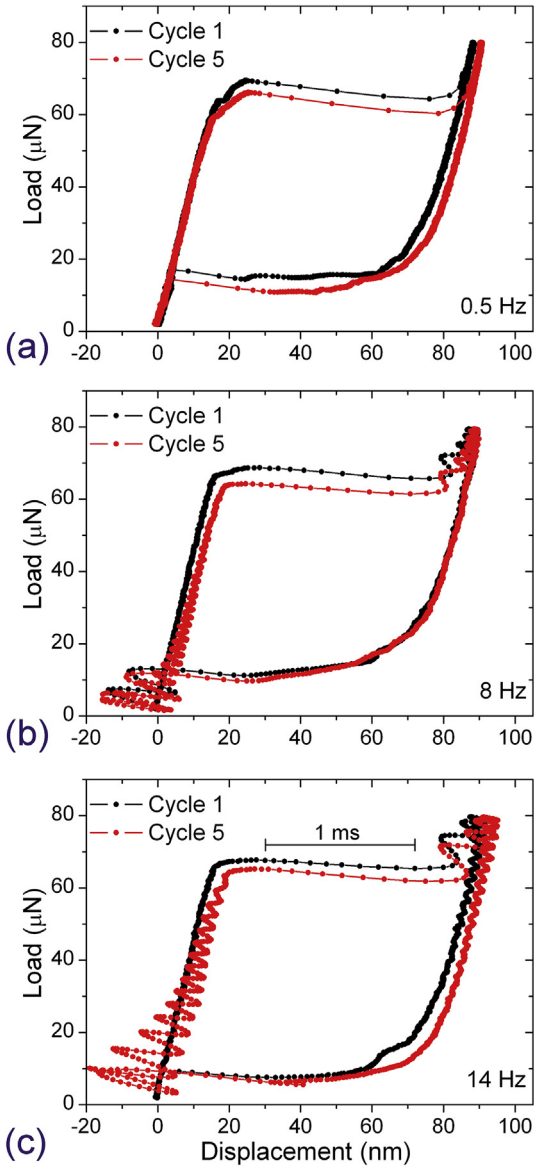

Fig. 9. (a) First and last superelastic cycles from a set of identical tests performed at 0.5 Hz on the pillar of Fig. 8a. (b), (c) Similar superelastic tests performed subsequently on the same pillar at 8 Hz and 14 Hz respectively. The total time elapsed along ten points, 10^{-3} s, is indicated, and oscillations due to the resonance of the transducer are clearly seen at high frequency in (b) and (c).

transformation, as indicated by the negative values of displacement. The frequency of the observed oscillations is related to the resonant frequency of the transducer, about 400 Hz, which prevents us from properly measuring superelastic cycles at higher frequencies. However, in spite of this experimental limitation, the superelastic cycle exhibits a reproducible, complete recovery, with a very high loss factor, $\eta = 0.23$ at 14 Hz, as well as an extremely fast superelastic response; the main part of the plateau in Fig. 9c, about 4% strain, takes place in 10^{-3} s. On the one hand, in these SMA the elastic waves velocity is about 2000 m s^{-1} [59], which means that the elastic response of the superelastic cycle can occur almost instantaneously at this time scale. On the other hand, the displacement velocity at the middle of the plateau is $v = 57 \times 10^3$ nm s^{-1} and the mean strain rate during the superelastic plateau is $\approx$ 40 s^{-1}. Taking into account that, even at macroscopic scale, superelastic strain rates one order of magnitude higher have

been observed [60], it could be considered that at small scale the superelastic response speed could be still increased by an order of magnitude, what means that a full cycle could occurs in 0.4×10^{-3} s. Thus, it can be reasonably estimated that a complete superelastic cycle could take place in less than 10^{-3} s, i.e., at a frequency as high as about 1000 Hz, ranging outside the measuring capabilities of the equipment.

Very large scale integration technologies used in integrated circuits and MEMS production are based on thin films planar technologies and typical Ti-Ni SMA thin films, grown by sputtering and used in MEMS, are ranging between 1 and 5 μm thickness, see Ref. [9] for a review. In the present study, the pillars of the array from Fig. 1 are 3.3 μm tall, but the smaller pillar from Fig. 8c is only 860 nm tall. This means that similar pillars could be milled by extensive FIB patterning, or produced by the classical lithography techniques used in MEMS technology, on SMA thin films from 1 to 5 μm thick. We can conclude that the observed superelastic damping could be translated to thin film structures to be used as dampers in MEMS. Consequently, it is expected that pillars or other features from these SMAs, fabricated in small volumes and integrated with MEMS devices, can offer an ultra-high loss factor in a range of frequencies useful for at least some applications, including the spacecraft applications described above.

4. Conclusion

In summary, micropillars of Cu-Al-Ni SMA exhibit a completely recoverable superelastic cycle, even up to 6% superelastic strain and spanning thousands of cycles and multiple years of interrupted testing. What is more, the stress-induced superelastic straining is highly dissipative, with these micropillars exhibiting an ultra-high mechanical damping loss factor $\eta > 0.1$ that remains stable over thousands of cycles, and which can become even higher, $\eta > 0.2$, when the size of the pillars is reduced into the nanometer range. Finally, the superelastic response is extremely fast, requiring only about 10^{-3} s for the full strain plateau to evolve, and the ultra-high damping is shown to be maintained at test frequencies up to at least 14 Hz, with a response signature that suggests similar behavior should persist even at frequencies as high as 1000 Hz. This range of frequencies is relevant, for instance, to the dominant range of mechanically transmitted spacecraft vibrations.

Consequently, we suggest that micro/nano pillar arrays or specifically designed micro/nano devices of Cu-Al-Ni SMA could constitute a novel solution to protect MEMS and NEMS against structural noisy vibrations and shocks, improving their reliability in many technological industrial sectors, and paving the way for the development of new generation of reliable smart MEMS devices.

Acknowledgements

This work was supported by the Spanish Ministry of Economy and Competitiveness, MINECO, projects MAT2012-36421, MAT2017–84069P, CONSOLIDER-INGENIO 2010 CSD2009-00013, as well as by the Consolidated Research Group IT-10-310 and the ELKARTEK-ACTIMAT project from the Education and Industry Departments of the Basque Government, Spain, and GIU-17/071 from the University of the Basque Country, UPV/EHU. Co-funding from H2020 REACT Project Grant Nº 640241 from European Community and EOARD Grant Nº FA8655-10-1-3074 (USA) are also acknowledged. This work made use of the FIB facilities of the SGIKER from the UPV/EHU. CAS acknowledges the support of the Institute for Soldier Nanotechnologies, funded by the U.S. Army Research Office at MIT, under contract number W911NF-13-D-0001.

Appendix A. Supplementary data

Supplementary data to this article can be found online at https://doi.org/10.1016/j.actamat.2018.12.043.

References

[1] L. Delaey, in: P. Haasen (Ed.), Materials Science and Technology Vol. 5, Phase Transformations in Materials, vol. 6, Wiley-VCH, Weinheim, Germany, 1991.
[2] K. Otsuka, C.M. Wayman (Eds.), Shape Memory Materials, Cambridge University Press, Cambridge, 1998.
[3] K. Yamauchi, I. Ohkata, K. Tsuchiya, S. Miyazaki (Eds.), Shape Memory and Superelastic Alloys, Woodhead Publishing, Cambridge, 2011.
[4] W.M. Huang, Z. Ding, C.C. Wang, J. Wei, Y. Zhao, H. Purnawali, Shape memory materials, Mater. Today 13 (2010) 54–61.
[5] J.M. Jani, M. Leary, A. Subic, M.A. Gibson, A review of shape memory alloy research, applications and opportunities, Mater. Des. 56 (2014) 1078–1113.
[6] J.V. Humbeeck, Shape memory alloys: a material and a technology, Adv. Eng. Mater. 3 (2001) 837–850.
[7] J.M. San Juan, M.L. Nó, C.A. Schuh, Superelasticity and shape memory in micro- and nanometer-scale pillars, Adv. Mater. 20 (2008) 272–278.
[8] M. Kohl, Shape Memory Microactuators, Springer, Berlin, 2004.
[9] S. Miyazaki, Y.Q. Fu, W.M. Huang (Eds.), Thin Film Shape Memory Alloys, Cambridge University Press, Cambridge, 2009.
[10] J. Cui, Y.S. Chu, O.O. Famodu, Y. Furuya, J. Hattick-Simpers, R.D. James, A. Ludwig, S. Thienhaus, M. Wuttig, Z. Zhang, I. Takeuchi, Combinatorial search of thermoelastic shape-memory alloys with extremely small hysteresis width, Nat. Mater. 5 (2006) 286–290.
[11] R. Zarnetta, R. Takahashi, M.L. Young, A. Savan, Y. Furuya, S. Thienhaus, B. Maass, M. Rahim, J. Frenzel, H. Brunken, Y.S. Chu, V. Srivastava, R.D. James, I. Takeuchi, G. Eggeler, A. Ludwig, Identification of quaternary shape memory alloys with near-zero thermal hysteresis and unprecedented functional stability, Adv. Funct. Mater. 20 (2010) 1917–1923.
[12] P.J.S. Buenconsejo, R. Zarnetta, D. König, A. Savan, S. Thienhaus, A. Ludwig, A new prototype two-phase (TiNi)–(β-W) SMA system with tailorable thermal hysteresis, Adv. Funct. Mater. 21 (2011) 113–118.
[13] C. Chluba, W. Ge, R.L. Miranda, J. Strobel, L. Kienle, E. Quandt, M. Wuttig, Ultralow-fatigue shape memory alloy films, Science 348 (2015) 1004–1007.
[14] H. Gu, L. Bumke, C. Chluba, E. Quandt, R.D. James, Phase engineering and supercompatibility of shape memory alloys, Mater. Today 21 (2018) 265–277.
[15] C.A. Schuh, Nanoindentation studies of materials, Mater. Today 9 (2006) 32–40.
[16] M.D. Uchic, D.M. Dimiduk, J.N. Florando, W.D. Nix, Sample dimensions influence strength and crystal plasticity, Science 305 (2004) 986–989.
[17] J.R. Greer, W.C. Oliver, W.D. Nix, Size dependence of mechanical properties of gold at the micron scale in the absence of strain gradients, Acta Mater. 53 (2005) 1821–1830.
[18] C.P. Frick, T.W. Lang, K. Spark, K. Gall, Stress-induced martensitic transformation and shape memory at nanometer scale, Acta Mater. 54 (2006) 2223–2234.
[19] J.M. San Juan, M.L. Nó, C.A. Schuh, Nanoscale shape-memory alloys for ultrahigh mechanical damping, Nat. Nanotechnol. 4 (2009) 415–419.
[20] D.C. Dunand, P. Müllner, Size effects on magnetic actuation in Ni-Mn-Ga shape-memory alloys, Adv. Mater. 23 (2011) 216–232.
[21] J.F. Gómez-Cortés, M.L. Nó, I. López-Ferreño, J. Hernández-Saz, S.I. Molina, A. Chuvilin, J.M. San Juan, Size effect and scaling power-law for superelasticity in shape memory alloys at the nanoscale, Nat. Nanotechnol. 12 (2017) 790–797.
[22] A.D. Romig, M.T. Dugger, P.J. McWhorter, Materials issues in microelectromechanical devices: science, engineering, manufacturing and reliability, Acta Mater. 51 (2003) 5837–5866.
[23] O. Tabata, T. Tsuchiya (Eds.), Reliability of MEMS, Wiley-VCH, Weinheim, 2008.
[24] N. Igata, K. Nishiyama, K. Ota, Y. Yin, W. Wuttig, I.S. Golovin, J.V. Humbeeck, J. San Juan, Panel discussion on the application of HDM, J. Alloy. Comp. 355 (2003) 230–240.
[25] J. San Juan, M.L. Nó, Damping behavior during martensitic transformation in shape memory alloys, J. Alloy. Comp. 355 (2003) 65–71.
[26] C.P. Frick, S. Orso, E. Arzt, Loss of pseudoelasticity in nickel–titanium submicron compression pillars, Acta Mater. 55 (2007) 3845–3855.
[27] C.P. Frick, B.G. Clark, A.S. Schneider, R. Maass, S.V. Petegem, H.V. Swygenhoven, On the plasticity of small-scale nickel-titanium shape memory alloys, Scripta Mater. 62 (2010) 492–495.
[28] B.G. Clark, D.S. Gianola, O. Kraft, C.P. Frick, Size independent shape memory behavior of nickel-titanium, Adv. Eng. Mater. 12 (2010) 808–815.
[29] J.R. Greer, J.T.M. De Hosson, Plasticity in small-sized metallic systems: intrinsic versus extrinsic size effect, Prog. Mater. Sci. 56 (2011) 654–724.
[30] J.M. San Juan, M.L. Nó, C.A. Schuh, Thermomechanical behavior at the nanoscale and size effects in shape memory alloys, J. Mater. Res. 26 (2011) 2461–2469.
[31] L. Liu, X. Ding, J. Li, T. Lookman, J. Sun, Direct observation of hierarchical nucleation of martensite and size-dependent superelasticity in shape memory alloys, Nanoscale 6 (2014) 2067–2072.

[32] Y. Chen, X. Zhang, D.C. Dunand, C.A. Schuh, Shape memory and superelasticity in polycrystalline Cu-Al-Ni microwires, Appl. Phys. Lett. 95 (2009) 171906.
[33] Y. Chen, C.A. Schuh, Size effects in shape memory alloy microwires, Acta Mater. 59 (2011) 537–553.
[34] S.M. Ueland, Y. Chen, C.A. Schuh, Oligocrystalline shape memory alloys, Adv. Funct. Mater. 22 (2012) 2094–2099.
[35] N. Tuncer, C.A. Schuh, Melt-cast microfibers of Cu-based shape memory alloy adopt a favorable texture for superelasticity, Scripta Mater. 117 (2016) 46–50.
[36] J. San Juan, M.L. Nó, C.A. Schuh, Superelastic cycling of Cu-Al-Ni shape memory alloy micropillars, Acta Mater. 60 (2012) 4093–4106.
[37] S.M. Ueland, C.A. Schuh, Superelasticity and fatigue in oligocrystalline shape memory alloy microwires, Acta Mater. 60 (2012) 282–292.
[38] J. San Juan, J.F. Gómez-Cortés, G.A. López, C. Jiao, M.L. Nó, Long-term superelastic cycling at nano-scale in Cu-Al-Ni shape memory alloy micropillars, Appl. Phys. Lett. 104 (2014), 011901.
[39] V. Recarte, R.B. Pérez-Sáez, E.H. Bocanegra, M.L. Nó, J. San Juan, Dependence of the martensitic transformation characteristics on concentration in Cu–Al–Ni shape memory alloys, Mater. Sci. Eng. A273–275 (1999) 380–384.
[40] O. Wilhelmi, H. Mulders, Focused ion beam and DualBeam™ technology applied to nanoprototyping, in: I. Utke, S. Moshkalev, P. Russell (Eds.), Nanofabrication Using Focused Ion and Electron Beams, Oxford Univ. Press, Oxford, 2012, pp. 380–409.
[41] J.I. Pérez-Landazabal, V. Recarte, R.B. Pérez-Sáez, M.L. Nó, J. Campo, J. San Juan, Determination of the next-nearest neighbor order in β phase in Cu-Al-Ni shape memory alloys, Appl. Phys. Lett. 81 (2002) 1794–1796.
[42] J. Ye, M. Tokonami, K. Otsuka, Crystal structure analysis of γ'_1 Cu-Al-Ni martensite using conventional X-rays and synchrotron radiations, Metall. Trans. A 21A (1990) 2669–2678.
[43] V. Novák, P. Sittner, N. Zárubová, Anisotropy of transformation characteristics memory alloys, Mater. Sci. Eng., A 234–236 (1997) 414–417.
[44] S.M. Ueland, C.A. Schuh, Transition from many domain to single domain martensite morphology in small-scale shape memory alloys, Acta Mater. 61 (2013) 5618–5625.
[45] G. Fantozzi, Mechanical spectroscopy: phenomenology and definitions, Mater. Sci. Forum 366–368 (2001) 3–31.
[46] R.S. Lakes, Viscoelastic Solids, CRC Press, Boca Raton, Fl, 1999.
[47] R. Schaller, High damping materials, Mater. Sci. Forum 366–368 (2001) 621–634.
[48] M.L. Nó, A. Ibarra, D. Caillard, J. San Juan, Quantitative analysis of stress-induced martensites by in situ transmission electron microscopy superelastic tests in Cu–Al–Ni shape memory alloys, Acta Mater. 58 (2010) 6181–6193.
[49] A. Ibarra, J. San Juan, E.H. Bocanegra, M.L. Nó, Evolution of microstructure and thermomechanical properties during superelastic compression cycling in Cu-Al-Ni single crystals, Acta Mater. 55 (2007) 4789–4798.
[50] M. Newell, Miniaturization of tuning forks, Science 161 (1968) 1320–1326.
[51] V. Kaajaraki, Practical MEMS, Small Gear Publishing, USA, 2009.
[52] C. Liu, Foundations of MEMS, Pearson Education Inc, Upper Saddle River, NJ, USA, 2006.
[53] J.A. Connally, S.B. Brown, Slow crack growth in single-crystal silicon, Science 256 (1992) 1537–1539.
[54] D.H. Alsem, O.N. Pierron, E.A. Stach, C.L. Muhlstein, R.O. Ritchie, Mechanisms for fatigue of micron-scale silicon structural films, Avd. Eng. Mater. 9 (2007) 15–30.
[55] Y.T. Cheng, Vacuum packaging technology, J. of MEMS 11 (2002) 556–565.
[56] R. Lagier, ARIANE 5 User's Manual, Issue 5 Revision 2, Arianspace, Evry-Courcouronnes, France, 2016.
[57] A. Calvi, Spacecraft Loads Analysis, ESA/ESTEC, Noordwijk, The Neetherlands, 2011.
[58] D. Kern, S. Gordon, Spacecraft & Launch Vehicle Dynamic Environments Workshop, NASA, USA, 2015.
[59] B. Graczykowski, S. Mielcarek, T. Breczewski, M.L. Nó, J. San Juan, B. Mroz, Martensitic phase transition in Cu-14%Al-4%Ni shape memory alloys studied by Brillouin light scattering, Smart Mater. Struct. 22 (2013) 085027.
[60] S. Nemat-Nasser, W.G. Guo, Superelastic and cyclic response of NiTi SMA at various strain rates and temperatures, Mech. Mater. 38 (2006) 463–474.